# Carrier Control of $MoS_2$ Nanoflakes by Functional Self-Assembled Monolayers

**Yang Li,[†] Cheng-Yan Xu,[†,‡,*] PingAn Hu,[‡] and Liang Zhen[†,‡,*]**

[†]School of Materials Science and Engineering, Harbin Institute of Technology, Harbin 150001, China and [‡]MOE Key Laboratory of Micro-systems and Micro-structures Manufacturing, Harbin Institute of Technology, Harbin 150080, China

## ABSTRACT

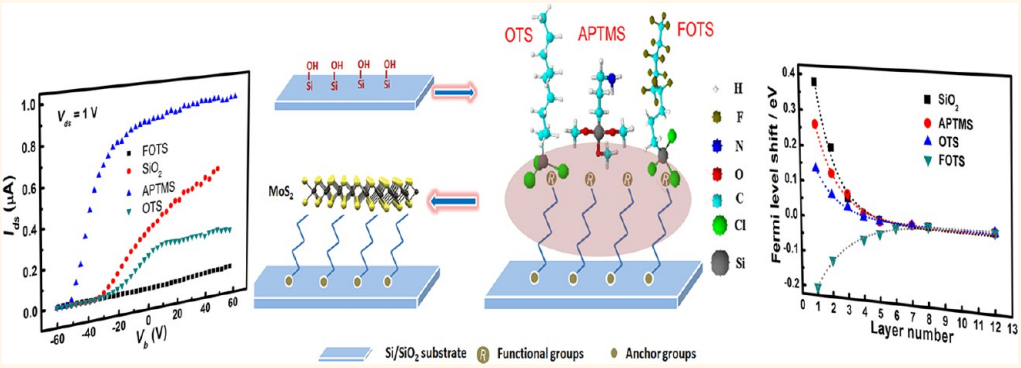


**Carrier doping of $MoS_2$ nanoflakes was achieved by functional self-assembled monolayers (SAMs) with different dipole moments. The effect of SAMs on the charge transfer between the substrates and $MoS_2$ nanoflakes was studied by Raman spectroscopy, field-effect transistor (FET) measurements, and Kelvin probe microscope (KFM). Raman data and FET results verified that fluoroalkyltrichlorosilane-SAM with a large positive dipole moment, acting as hole donors, significantly reduced the intrinsic *n*-doping characteristic of $MoS_2$ nanoflakes, while 3-(trimethoxysilyl)-1-propanamine-SAMs, acting as electron donors, enhanced the *n*-doping characteristic. The additional built-in electric field at the interface between $SiO_2$ substrates and $MoS_2$ nanoflakes induced by SAMs with molecular dipole moments determined the charge transfer process. KFM results clearly demonstrated the charge transfer between $MoS_2$ and SAMs and the obvious interlayer screening effect of the pristine and SAM-modified $MoS_2$ nanoflakes. However, the KFM results were not fully consistent with the Raman and FET results since the externally absorbed water molecules were shown to partially shield the actual surface potential measurement. By eliminating the contribution of the water molecules, the Fermi level of monolayer $MoS_2$ could be estimated to modulate in a range of more than 0.45—0.47 eV. This work manifests that the work function of $MoS_2$ nanoflakes can be significantly tuned by SAMs by virtue of affecting the electrostatic potential between the substrates and $MoS_2$ nanoflakes.**

**KEYWORDS:** $MoS_2$ nanoflakes · self-assembled monolayer · surface potential · charge transfer · Kelvin probe microscopy

Transition metal dichalcogenides (TMDs) have been receiving considerable attention since they present a wide range of electronic, optical, mechanical, and thermal properties.[1,2] In the past few years, as significant layered semiconductor nanomaterials, monolayer or few-layer TMDs nanoflakes have been extensively investigated, and they are also regarded as perfect candidates for future electronic devices.[3−5] Because of the easy exfoliation from natural crystals, molybdenum disulfide ($MoS_2$), a representative TMD, attracted great scientific and engineering interest most recently.[6,7] $MoS_2$ crystals are composed of S−Mo−S units, stacked with each other *via* van der Waals interaction. Bulk $MoS_2$ has an indirect bandgap of 1.2 eV, while monolayer $MoS_2$ presents suitable direct bandgap of 1.8 eV.[8] Since the bandgap of $MoS_2$ nanoflakes varies with their thicknesses, $MoS_2$ nanoflakes with different thicknesses exhibit excellent photodetection in a wide range of spectral responses from UV to near IR.[9−12] On the nanoscale, the electrical contacts play an important role in the performance of functional nanodevices based on $MoS_2$ nanoflakes.[13] Therefore, in order to control the contact barriers, the work function of $MoS_2$ nanoflakes with different layers should be essentially considered to modulate the energy level alignment at the interface between $MoS_2$ and metal electrodes. According to references,[14−18] contact resistance induced by Schottky barriers

* Address correspondence to lzhen@hit.edu.cn, cy_xu@hit.edu.cn.

Received for review May 28, 2013 and accepted August 16, 2013.

**Published online August 16, 2013**
**10.1021/nn402682j**

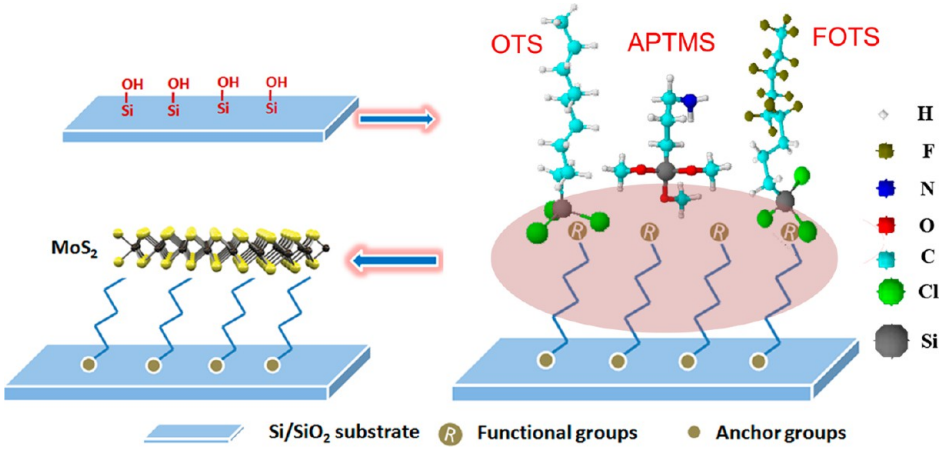


**Figure 1. Schematic illustration of modifying $SiO_2$ substrates with functional self-assembled monolayers. Three kinds of silane coupling agents were used: octyltrichlorosilane ($C_8H_{17}SiCl_3$); 3-(trimethoxysilyl)-1-propanamine ($NH_2(CH_2)_3Si(OCH_3)_3$); and trichloro(1*H*,1*H*,2*H*,2*H*-perfluorooctyl)silane ($CF_3(CF_2)_5CH_2CH_2SiCl_3$).**

impedes the charge transfer at electrical contacts, thereby lowering the performance of $MoS_2$ devices. A few reports have concentrated on tuning the charge transfer and lowering the contact barriers at the electrical contacts by choosing metal electrodes with appropriate work function.[14−17] Recently, the interlayer screening effect of $MoS_2$ nanoflakes has been demonstrated and the work function of $MoS_2$ nanoflakes varied with the number of layers.[19,20] However, the lack of active modulation of the work function of $MoS_2$ nanoflakes hinders the optimization of electrical contacts.

Self-assembled monolayers (SAMs) of organic molecules are ultrathin molecular films, which are spontaneously constructed at the interface between the substrates and organosilanes through chemical or physical reactions.[21−23] During the past few decades, SAMs have attracted technological attention for surface and interface engineering since they can easily tune the surface energy, dipole moment, and chemical reactivity of the surface by functional groups.[22,23] As a buffer layer, SAMs have been used to tune the work function of graphene and the energy level alignment of organic nanodevices by modulating the holes or electron injection.[24−30] Because of the atomic thickness of two-dimensional nanoflakes (such as graphene and $MoS_2$), the charge transfer between functional SAMs and nanoflakes may be more significant and effective, and it is expected to effectively tune the work function of ultrathin nanoflakes by SAMs. In this work, we tuned the work function of $MoS_2$ nanoflakes by modifying $SiO_2$ substrates with functional SAMs with different dipole moments. SAMs were successfully formed on $SiO_2$ substrates, which were characterized by atomic force microscope (AFM) and X-ray photoelectron spectroscopy (XPS). The effects of SAMs on charge carrier modulation of $MoS_2$ nanoflakes were investigated by Raman spectroscopy, field-effect transistor (FET) measurements and Kelvin probe microscope (KFM). Raman spectra and FET results have demonstrated the carrier modulation of $MoS_2$ induced by self-assembled monolayers. KFM successfully demonstrated the charge transfer between $MoS_2$ and SAMs and the obvious interlayer screening effect of the pristine and SAM-modified $MoS_2$ nanoflakes. In order to eliminate the effect of the water molecules, humidity and annealing experiments were conducted to amend the KFM results.

## RESULTS AND DISCUSSION

The schematic illustration of sample preparations is shown in Figure 1. First, $p^{++}$ silicon wafer with a 300 nm-thick thermal oxide layer was cleaned by piranha solution in order to remove the residues and make the wafer covered with hydroxyl group (−SiOH). Then the silicon substrates were dipped into the solution containing silane coupling agents for several hours; thus, SAMs could be formed spontaneously at the solid−liquid interface through the reaction with hydroxyl group through cross-linking.[22] Three kinds of silane coupling agents, octyltrichlorosilane (OTS, $CH_3$−SAM), 3-(trimethoxysilyl)-1-propanamine (APTMS, $NH_2$−SAM), and trichloro(1*H*,1*H*,2*H*,2*H*-perfluorooctyl)silane (FOTS, $CF_3$−SAM), were chosen in our experiments with the consideration of their different dipole moments and polarities.[29,31] Generally, $CH_3$-terminated SAMs have little contribution to carrier doping due to the slight dipole moment. SAMs with $NH_2$-functional group have lone pair electrons, and these groups exhibit electron-donating characteristics. Because of the large electronegativity of F atoms, $CF_3$−SAMs have large hole-doping ability. Subsequently, $MoS_2$ nanoflakes were transferred to SAM-modified substrates by mechanical exfoliation from bulk $MoS_2$ crystals.

To reveal the components of SAMs, XPS analysis was first conducted to characterize the chemical states of elements contained in SAMs. The binding energy for each sample was calibrated by the peaks at 103.6 and 532.8 eV, originating from Si2p and O1s of the pristine $SiO_2$ substrate, respectively. All the peaks on the survey

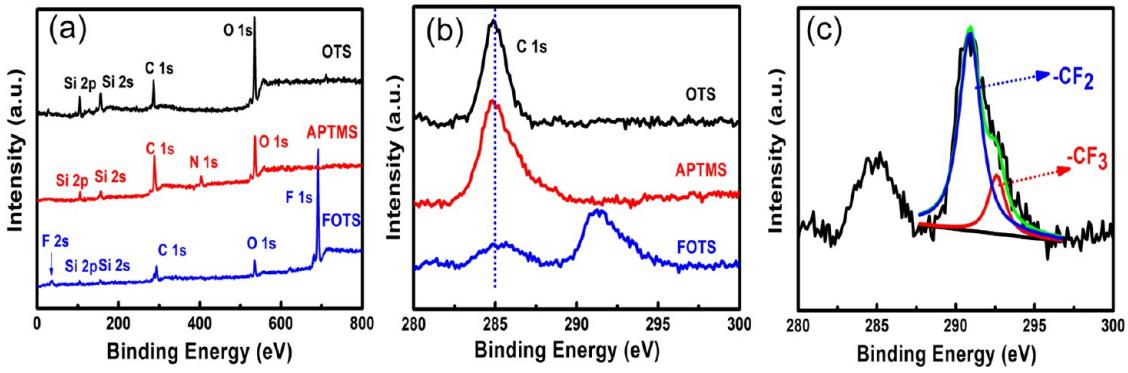


**Figure 2. XPS spectra for OTS, APTMS, and FOTS SAMs. (a) Survey spectra within the range of 0−800 eV. (b) High resolution spectra of C1s peak for three SAMs. (c) The fitting (−$CF_2$− and −$CF_3$−) spectra of C1s peak for FOTS.**

spectra of three SAMs in the range of 0−800 eV were assigned to their corresponding elements contained in each SAMs molecule, as shown in Figure 2a.

The N1s in APTMS and F1s in FOTS are located at 401.2 and 688 eV respectively. The absence of chlorine signal in FOTS indicates the complete hydrolysis of chlorine, and the byproducts were removed by the washing process.[31] The chemical state of carbon atoms in three kinds of SAM molecules was examined, and the obvious chemical shifts of C1s were observed, as presented in Figure 2b. The C atoms in OTS are composed of −$CH_2$, and the C1s in OTS was assigned to carbon in −$CH_2$. Likewise, the C atoms in APTMS are also composed of −$CH_2$; therefore, the C1s peak has little shift compared to the C1s in OTS, locating at about 285.0 eV. However, C1s peak in FOTS has larger positive chemical shifts than C1s from −$CH_2$, which stems form the strong electronegativity of F atoms.[30,32] Because of the presence of −$CF_2$ and −$CF_3$ groups, the C1s peaks in FOTS contain three components through deconvolution: one at 285 eV denoting −$CH_2$ group, another at 291.8 eV denoting −$CF_2$ group, and the third at 293.1 eV denoting −$CF_3$ group.[33] By calculating the fitted areas of C−F peak in Figure 2c, the carbon content ratio of −$CF_2$ to −$CF_3$ is about 4.48, lower than the original −$CF_2$/−$CF_3$ = 5 in the molecules of FOTS, which may be caused by the decomposition of C−F bonds irradiated by X-ray during the XPS measurements.

Further, we used AFM to characterize the topographies of SAMs, as shown in Figure 3. It should be noted that it is easier to introduce the large bulges (see Figure 3b,c) because of the cross-link reactions with other SAMs precursors when self-assembled monolayers are fabricated in liquid atmosphere. The AFM topography of OTS SAM is shown in Figure 3a. OTS is composed of island-like aggregates, leading to a relatively rough surface.[34,35] Generally speaking, OTS reacts directly with the OH group on silicon oxide surface, but it appeared to be hydrolyzed easily and, as a consequence, reacted with other OTS molecules to form large and island-like aggregates.[34] As shown in Figure 3b, compact APTMS film with relatively nonuniform bulges was formed. The large bulges may be caused by the activity of the terminated $NH_2$ group: it can react with Si−OH and Si−$(OH)_3$ (the headgroup of hydrolyzed APTMS molecules in the presence of absorbed water molecules).[36] Note that since the hydrolysis of FOTS is quick because of the sensitivity to small amounts of water, it is difficult to control the formation of FOTS SAM.[37] In Figure 3c, it can be seen that the substrate was not fully covered with FOTS, while FOTS was relatively flat. From the topographic profile in the inset of Figure 3c, the thickness of FOTS SAM is approximately 1.3 nm, which is consistent with the height of a single FOTS molecule.[31] The roughnesses of $SiO_2$, OTS, APTMS, and FOTS are 0.46, 0.86, 0.54, and 0.63 nm, respectively. The contact angle of silicon oxide substrate modified by piranha solution is less than 30° (see Figure S1b, Supporting Information), indicating that the substrates were perfectly covered with hydroxyl group (−OH). Through measuring the wettability of SAMs, the water contact angles are about 53°, 109°, and 120° for APTMS, OTS, and FOTS, respectively, as shown in Figure 3d, indicating that APTMS is hydrophilic while OTS and FOTS are hydrophobic, consistent with previous works.[36,38]

After transferring $MoS_2$ nanoflakes onto the SAM-modified $SiO_2$ substrates, we intended to conduct Raman spectra to study the effects of SAMs on the resonance modes of $MoS_2$ nanoflakes ($E_{2g}^1$ and $A_{1g}$). For $MoS_2$ nanoflakes with different thickness, the out-of-plane mode $E_{2g}^1$ presents a red shift with increasing thicknesses, while the in-plane $A_{1g}$ shows a blue shift (see Figure S2a, Supporting Information), which can be explained in terms of enhanced dielectric screening of long-range Coulomb interaction between the effective charges.[39] Then, we quantitatively compared the Raman features of monolayer $MoS_2$ on the pristine $SiO_2$ substrate with the counterparts on the SAM-modified substrates, as shown in Figure 4a. In comparison with monolayer $MoS_2$ on the pristine $SiO_2$ substrate (as a reference), both resonance modes $A_{1g}$ and $E_{2g}^1$ of monolayer $MoS_2$ on the OTS-modified substrate show unnoticeable changes, indicating that OTS SAM has

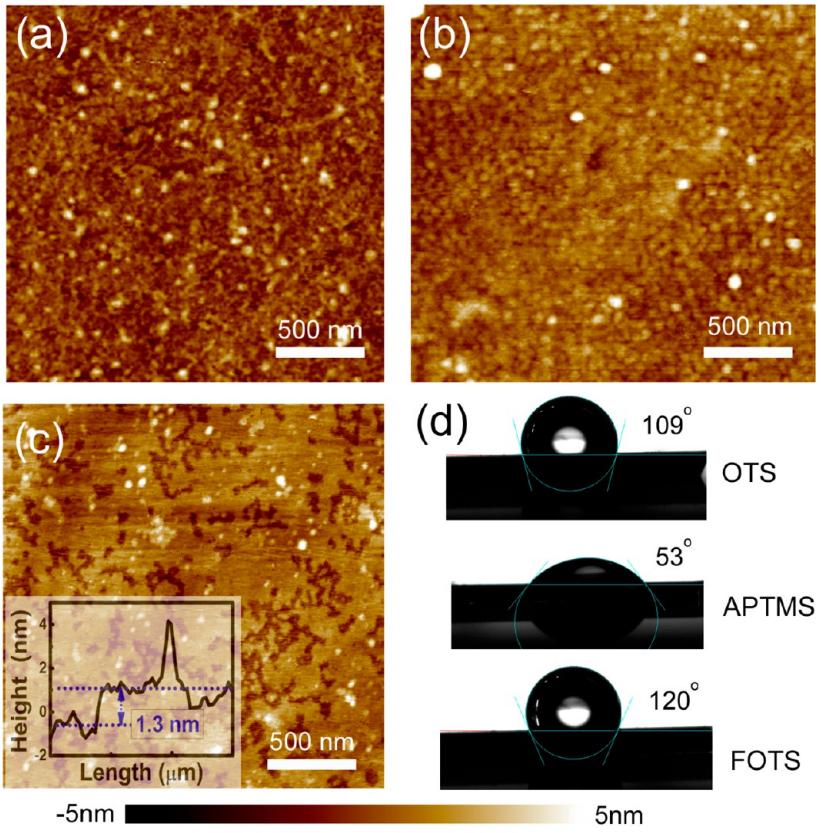


**Figure 3. Typical AFM topographies and water contact angles of three kinds of self-assembled monolayers. (a−c) Topographies of OTS, APTMS, and FOTS SAMs on $SiO_2$ substrates, respectively. (d) Water contact angles of three kinds of SAMs.**

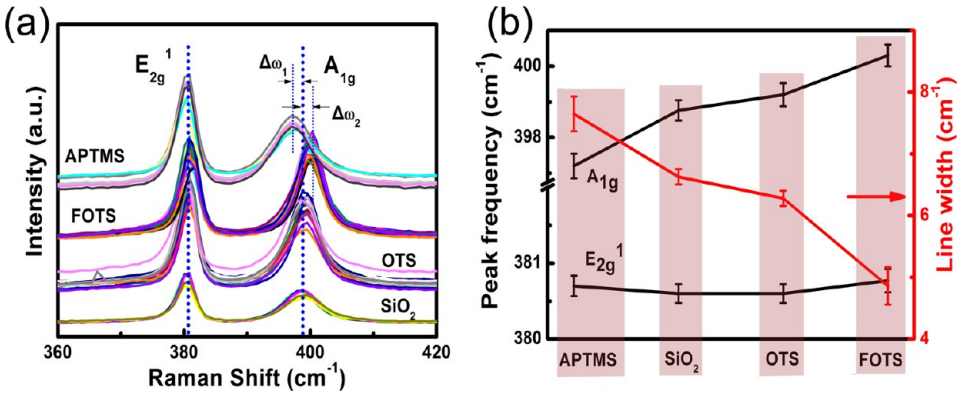


**Figure 4. (a) Raman spectra of monolayer $MoS_2$ on the pristine and SAM-modified $SiO_2$ substrates. (b) Peak frequencies of $A_{1g}$ and $E_{2g}^1$ modes (left *Y* axis) and line width of $A_{1g}$ mode (right *Y* axis) of monolayer $MoS_2$ on the pristine and SAM-modified $SiO_2$ substrates.**

little effect on carrier transfer between monolayer $MoS_2$ and OTS. However, $A_{1g}$ mode of monolayer $MoS_2$ on the FOTS- and APTMS-modified substrates presents blue shift by 1.7 $cm^{-1}$ and red shift by 1.6 $cm^{-1}$, respectively. Note that the spectral resolution is about 0.5 $cm^{-1}$, and the blue shift and red shift of $A_{1g}$ mode indeed reflect the distinct hole doping and electron doping, respectively. In contrast, the $E_{2g}^1$ mode of monolayer $MoS_2$ on SAM-modified substrates keeps almost constant regardless of doping or undoping. The line width of $A_{1g}$ mode decreased by hole doping, while it increased by electron doping, as shown in Figure 4b. Considering that the strain can also induce the shift and split of $E_{2g}^1$ mode, and has unnoticeable effect on $A_{1g}$ mode, which is verified by theoretical and experimental results,[40,41] we deduce that charge doping is attributed to the observed Raman shift of $A_{1g}$ since the Raman shift of resonance modes induced by strain is not consistent with the experimental observation in our work. Chakraborty[42,43] has demonstrated that the occupation of the bottom of the conduction band at K-point states caused by

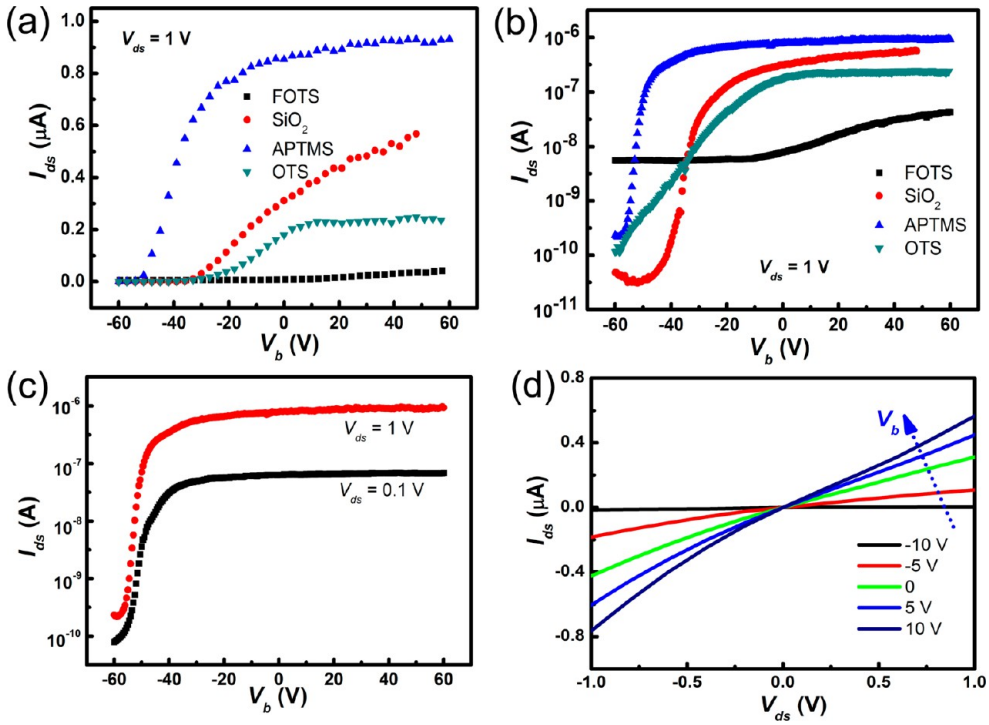


**Figure 5. (a) Transfer characteristics of few-layer $MoS_2$ nanoflakes (typical trilayer $MoS_2$ in our works) on pristine and SAM-modified $SiO_2$ substrates. (b) The corresponding semilog plots of $I_{ds}$ *versus* $V_b$ for the devices with different SAMs treatment. (c) Transfer characteristics of few-layer $MoS_2$ nanoflake on APTMS-modified substrates at $V_{ds}$ = 0.1 and 1 V, respectively. (d) The output characteristics of the corresponding device modified by APTMS.**

electron doping was attributed to a significant change in the electron−phonon coupling of the $A_{1g}$ mode, while the phonon of $E_{2g}{}^1$ mode is weakly dependent on doping. The effect of hole doping on $A_{1g}$ mode is similar. Since FOTS extracts electrons from $MoS_2$ monolayer, the carrier density decreases by $7.65 \times 10^{12}$ $cm^{-2}$, while the carrier density of $MoS_2$ monolayer on APTMS-modified substrate increases by about $7.2 \times 10^{12}$ $cm^{-2}$. It should be noted that though bilayer or trilayer $MoS_2$ on these substrates were also doped by SAMs (which will be described by KFM technique in the following part), the $A_{1g}$ mode of bilayer or trilayer $MoS_2$ did not present any changes (see Figure S2d, Supporting Information). Compared with monolayer $MoS_2$, the effects of SAMs on few-layer $MoS_2$ may be mitigated because of the interlayer screening effects but cannot be fully screened, which will be demonstrated by KFM and FET measurements. Considering that the sensitivity of Raman spectroscopy and the relatively weak doping effects compared with monolayer $MoS_2$, it is difficult to detect the charge doping effects of SAMs on few-layer $MoS_2$ by Raman spectroscopy.

To evaluate the doping effects of SAMs, the transport properties of few-layer $MoS_2$ FETs on different SAMs were measured. In our work, the measured $MoS_2$ nanoflakes were about 3 layers, as shown in Figure S3c, Supporting Information, and the channel length was 6 $\mu$m. The devices were annealed at 150 °C for 4 h in Ar atmosphere. Figure 5 displays the device characteristics of few-layer $MoS_2$ nanoflakes FETs; Figure 5a and b present the source-drain current ($I_{ds}$) against the gate voltage ($V_b$) in a linear and logarithmic scale, at a constant source-drain voltage of $V_{ds}$ = 1 V for pristine and SAM-modified devices. For the $MoS_2$ FET on FOTS, the obvious positive threshold voltage ($V_{th}$) shift is observed, indicating that the *n*-doping characteristic is mitigated. For the device made on $NH_2$−SAMs, the $V_{th}$ is downshifted, suggesting that $NH_2$−SAM has a relatively strong electron-doping effect. Figure 5a shows that $I_{ds}$ distinctly depends on the SAMs molecules. The $I_{ds}$ for APTMS-modified devices is much higher than that of FOTS, and the ON/OFF ratio of ATPMS-modified devices is higher than $10^3$, while that of FOTS-modified devices is less than 10, indicating that the carrier concentration is significantly decreased by inserting SAMs molecules. Figure 5c and d shows the typical transfer and output characteristics of APTMS-modified devices. $I_{ds} - V_{ds}$ presents nearly linear, indicating the lower contact resistance between Al electrodes and few-layer $MoS_2$. The corresponding transfer and output curves of FOTS-modified devices are shown in Figure S3, Supporting Information. The carrier mobilities can be estimated on the basis of the equation[9]

$$\mu = \frac{L}{W \times (\varepsilon_0 \varepsilon_r / d) \times V_{ds}} \times \frac{dI_{ds}}{dV_b}$$

where $L$, $W$, and $d$ are the channel length, width, and the thickness of $SiO_2$ (300 nm in our devices), and $\varepsilon_r$ for $SiO_2$ is 3.9. The carrier mobilities for pristine, APTMS-, OTS-, and FOTS-modified devices are 2.06 ± 0.32, 3.47 ± 0.36,

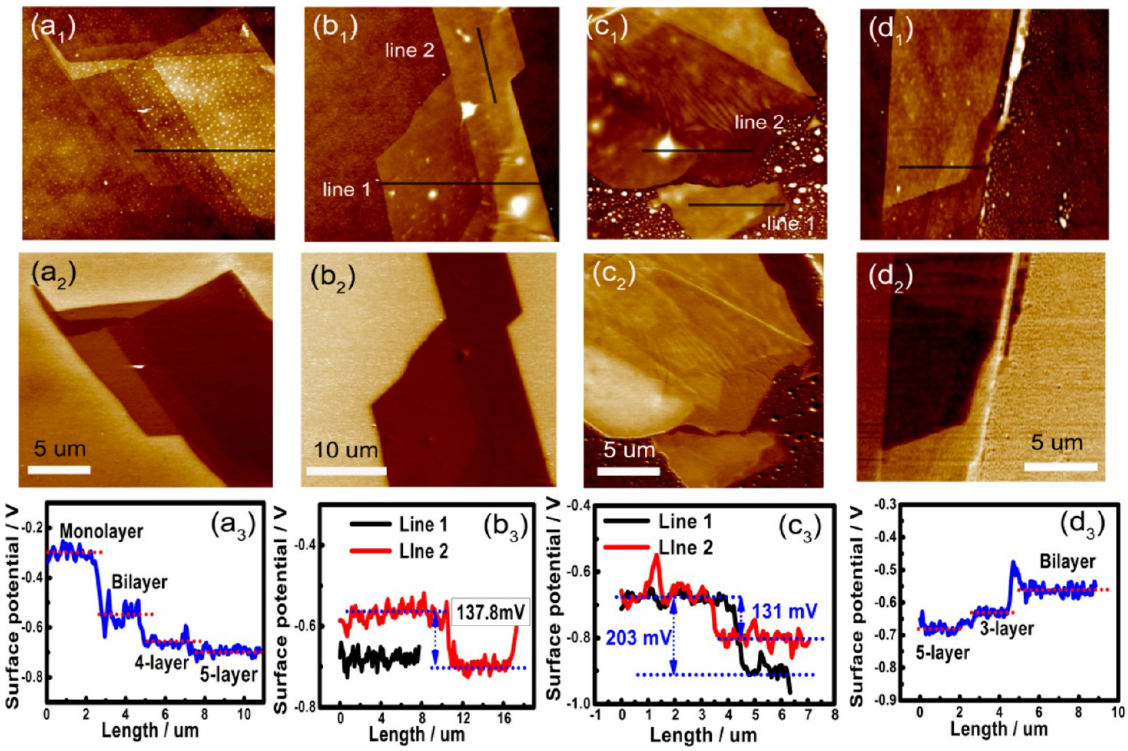


**Figure 6. AFM topographies and surface potential maps of $MoS_2$ nanoflakes on the pristine and SAM-modified $SiO_2$ substrates. ($a_1$−$d_1$) The topographies of $MoS_2$ nanoflakes on the $SiO_2$, OTS, FOTS, and APTMS. ($a_2$−$d_2$) The corresponding surface potential maps of $MoS_2$ nanoflakes shown in Figure 5$a_1$−$d_1$. ($a_3$−$d_3$) The potential profiles of $MoS_2$ nanoflakes according to the potential maps shown in Figure 5$a_2$−$d_2$.**

1.82 ± 0.45, and 0.087 $cm^2/(V\ s)$, respectively. The carrier mobility of FOTS-modified device is much lower than that for other SAM-treated FETs, while the carrier mobility of $CH_3$-modified device is relatively lower than that of pristine $MoS_2$ device. The results verify that electrons and holes tend to be accumulated for $NH_2$− and $CF_3$−SAMs because of the significant dipole moments, while there is no distinct effect on carrier accumulation for $CH_3$−SAM. Although the previous references reported that the carrier mobility of $CH_3$-modifed graphene FET was larger than untreated graphene-FETs because of the reduced Coulomb scattering,[44,45] the phenomena is not observed for OTS-modified $MoS_2$ devices compared with pristine $MoS_2$ devices, which may stem from the relative large roughness of modified substrates. Furthermore, we calculate the charge concentration ($n$) using the parallel-plate capacitor model with $n = C\Delta V_b/e$, where $C = \varepsilon_0\varepsilon_r/d$, $\varepsilon_0 = 8.85 \times 10^{-12}$ F/m, $\varepsilon_r = 3.9$, $d = 300$ nm (the thickness of $SiO_2$), $\Delta V_b = V_b - V_{th}$. When $V_b = 40$ V, $n$ of APTMS and FOTS-modified trilayer $MoS_2$ devices are calculated to be $5.6 \times 10^{12}$ and $3.4 \times 10^{12}$ $cm^{-2}$, respectively. It is shown that for trilayer $MoS_2$, the doped carrier density induced by SAMs can be modulated in the range of $2.2 \times 10^{12}$ $cm^{-2}$. Considering the relatively strong interlayer screening effect and the easily screened built-in electric field induced by SAMs, the doping concentration for monolayer $MoS_2$ should be higher than $2.2 \times 10^{12}$ $cm^{-2}$, which is consistent with the Raman results. By combining with FET and Raman results, we infer that the monolayer $MoS_2$ on FOTS may be transferred to *p*-doping completely, which will be demonstrated by KFM results. The effects of SAMs on the electronic properties of materials have been extensively investigated. Charge transfer between SAMs and $MoS_2$ under the additional built-in electric field at the interface induced by SAMs with molecular dipole moments is attributed to the carrier modulation of $MoS_2$ nanoflakes.

KFM has been widely used to characterize the spatial charges distribution of graphene doped by SAMs.[28,46] To investigate the charge transfer between $MoS_2$ nanoflakes and SAMs, surface potential of $MoS_2$ nanoflakes on the pristine and SAM-modified $SiO_2$ substrates was characterized by KFM. Figure 6$a_1$−$d_1$ shows AFM topographies of $MoS_2$ nanoflakes on the pristine $SiO_2$, OTS-, FOTS-, and APTMS-modified substrates, respectively. According to optical microscope observation, the layer number of $MoS_2$ nanoflakes can be distinguished (see Figures S4 and S5, Supporting Information). Figure 6$a_2$−$d_2$ presents the corresponding surface potential (SP) images. Obvious contact potential difference (CPD) between $MoS_2$ nanoflakes with different number of layers is observed on all four substrates. The potential profiles acquired from potential images are shown in Figure 6$a_3$−$d_3$. For $MoS_2$ nanoflakes on the pristine $SiO_2$ substrate, the surface potential of monolayer, bilayer, triple-layer, and 5-layer are −0.3, −0.52, −0.67, and −0.7 V, respectively (Figure 6$a_3$). For $MoS_2$ nanoflakes on the OTS-modified substrate, the contact potential difference

(CPD) between monolayer and bilayer $MoS_2$ nanoflakes is 137.8 mV, while the CPD between bi-, triple-, or multiple-layer $MoS_2$ nanoflakes presents subtle changes (Figure Figure 6b$_3$). For $MoS_2$ nanoflakes on the FOTS-modified substrate, the CPD between bilayer and 5-layer $MoS_2$ is 131 mV, while the CPD between monolayer and 8-layer $MoS_2$ is 203 mV (Figure 6c$_3$). For $MoS_2$ nanoflakes on the APTMS-modified substrate, the bilayer, triple-layer, and 5-layer $MoS_2$ are −0.55, −0.63, and −0.68 V, respectively (Figure 6d$_3$). Generally, the surface potential of $MoS_2$ nanoflakes decreases with increasing thickness for pristine $SiO_2$, OTS-, and APTMS-modified substrates. However, for the FOTS-modified substrate, the surface potential increases with the number of layers. Compared with contact potential difference between AFM tip and SAMs, the surface potential of different SAMs is that $SP_{APTMS} < SP_{OTS} < SP_{FOTS}$. According to Helmholtz equation[47] $\Delta V_{SAM_1-SAM_2} = (N(\mu_{SAM_1} - \mu_{SAM_2}) \cos\theta)/(\varepsilon_0\varepsilon_r)$, where $\Delta V$, $N$, and $\mu$ are the surface potential difference of SAMs, the dipole density, and the dipole moment, respectively, we infer that the order of dipole moments of these SAMs is $\mu_{APTMS} < \mu_{OTS} < \mu_{FOTS}$, which is in good accordance with the references.[48,49] The observed work function difference between SAMs can be attributed to the different intrinsic molecular dipole moments.

The Fermi level shift ($E_{\Delta F}$) denotes the work function difference between $MoS_2$ nanoflakes and bulk $MoS_2$, and can be calculated by $E_{\Delta F} = W_{MoS_2} - W_{bulk}$, where $W_{MoS_2}$ and $W_{bulk}$ are the work function of $MoS_2$ nanoflakes and *bulk* $MoS_2$, respectively. As described in the case of graphene/SAMs, the electric field induced by the charge transfer at the interface is short-ranged and can be easily screened as the thickness increases.[30,50] As demonstrated by previous work,[19,20] the interlayer screening effect also exists in $MoS_2$ nanoflakes and electric field also can be screened when the thickness of $MoS_2$ nanoflakes increases to 7 nm or more. Therefore, we consider $MoS_2$ nanoflakes with 12 layers as *bulk* $MoS_2$ and also measured the dependence of Fermi level shift on the number of layers. By measuring more than six $MoS_2$ nanoflakes on the pristine and SAM-modified substrates, the dependence of Fermi level shifts on layer numbers is presented in Figure 7. The Fermi level shift of $MoS_2$ on the pristine $SiO_2$, OTS-, and APTMS-modified substrates decreases monotonically with increasing the layer number, approaching a limit for $MoS_2$ containing several layers. Moreover, the Fermi level shift of $MoS_2$ on FOTS increases monotonously with the layer number, suggesting that the holes are injected into $MoS_2$ significantly. Regardless of the pristine or SAM-modified $MoS_2$ nanoflakes, the distinct interlayer screening effects are observed, demonstrating that the electrostatic potential induced by SAMs can be also screened through the layer-by-layer charge distribution within a few layers.

Compared with Raman data and FET results, the variation of surface potential of $MoS_2$ nanoflakes dependent on

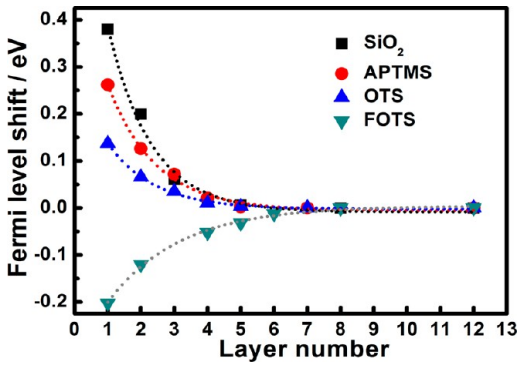


**Figure 7. The Fermi level shift of $MoS_2$ nanoflakes on various substrates as a function of the number of layers. The fitted lines indicate exponential decrease (for the pristine $SiO_2$, OTS- and APTMS-modified substrates) and increase for the FOTS-modified subtrate.**

SAMs with different dipole moments seems to be not fully consistent with the former two results, where the monolayer $MoS_2$ on the pristine $SiO_2$ substrates seems to be more *n*-doping than that on the APTMS-modified substrates. Since $MoS_2$ has significant hydrophility and can easily absorb the water molecules, the absorbed water molecules may shield the measurement of actual surface potential,[51,52] which has been demonstrated for both graphene and BN nanoflakes.[53,54] Therefore, we hypothesize that the external absorbed water molecules impede the measurement of surface potential of $MoS_2$, leading to the inconsistent phenomenon with Raman spectra and FETs results. To verify this, the surface potential of $MoS_2$ nanoflakes with different humidity and annealing is measured by KFM (see Figures S7−11, Supporting Information). Compared with the pristine samples, the surface potential of annealed $MoS_2$ nanoflakes decreases obviously (for monolayer $MoS_2$ on pristine and SAM-modified substrates, it decreases by about 0.10−0.12 V), and the interlayer screening effects become weaker, as shown in Figures S7 and S8, Supporting Information. However, the surface potential seems to have little variation when the humidity increases (see Figures S10 and S11, Supporting Information). The above results demonstrate that the externally absorbed water layers or molecules indeed shield the actual surface potential measurement for $MoS_2$ nanoflakes because of the significant hydrophility, and KFM may be not the most reliable tool to exactly reflect the intrinsic charge transfer process between SAMs and $MoS_2$ nanoflakes. Therefore, by eliminating the contribution of the absorbed water layers or molecules, we calibrate that the actual Fermi level shift of monolayer $MoS_2$ is about 0.45−0.47 eV.

## CONCLUSIONS

In summary, we have investigated the carrier control of $MoS_2$ nanoflakes by self-assembled monolayers with different functional groups. Raman spectra and FETs measurements have demonstrated that FOTS with large positive dipole moments, acting as hole donors,

significantly mitigated the intrinsic *n*-doping characteristic, while ATPMS with a negative dipole moment, acting as electron donors, enhanced the *n*-doping characteristic. By measuring the Fermi level shifts of $MoS_2$ nanoflakes on the pristine and SAM-modified $SiO_2$ substrates, we found that SAMs indeed affect the carrier distribution and the charge transfer process between $MoS_2$ and SAMs molecules, and the distinct interlayer screening effects still existed. By carrying out humidity and annealing experiments, it was demonstrated that the externally absorbed water molecules partially shield the measurement of actual surface potential, leading to the inconsistency of the Raman data, FET, and KFM results. By eliminating the contribution of the water molecules, the work function of monolayer $MoS_2$ could be estimated to modulate in a range of 0.45−0.47 eV. The results in this work show that in order to improve the performance of $MoS_2$-based nanodevices, exploring the modulation of work function of $MoS_2$ nanoflakes by self-assembled monolayers is essential to tune the energy level alignment at the electrical contacts and to control the contact barriers.

## EXPERIMENTAL METHODS

**Preparation of Silicon Oxide Surface.** Before the formation of SAMs, silicon substrate with a 300 nm oxide layer was treated by piranha solution (7:3 v:v sulfuric acid to hydrogen peroxide) at 100 °C for 30 min in order to remove residual organic contaminates and make the surface of $SiO_2$ hydrophilic. Then, the substrates were washed by deionized water for several times.

**Formation of SAMs.** Three kinds of silanes, ($CH_3$-terminated) octyltrichlorosilane (OTS), ($NH_2$-terminated) 3-(trimethoxysilyl)-1-propanamine (APTMS), and ($CF_3$-terminated) trichloro-(1*H*,1*H*,2*H*,2*H*-perfluorooctyl)silane (FOTS), were purchased from Sigma-Aldrich. For the formation of OTS and APTMS SAMs, the substrates were immerged into the silane/toluene mix solution (1:100 v:v) for 2 h and 30 min, respectively. For FOTS SAMs, the substrates were immerged into the silane/*n*-hexadecane (1:1000 v:v) for 30 min. After the film deposition, the substrates were rinsed by toluene, acetone, and alcohol successively for several times and then baked at 120 °C for 20 min.

**Characterization of SAMs.** Water contact angle was measured by placing deionized water droplet on the surface of substrate modified with SAMs. Four measurements on each sample were recorded. The elementary compositions of SAMs were characterized by XPS (PHI 5700 ESCA System with Al Kα). The morphologies of SAMs were measured by a scanning probe microscope (SPM, Bruker Dimension Icon).

**Raman Spectrometry.** Raman spectroscope at the excitation wavelength of 532 nm was used. The laser beam was focused onto $MoS_2$ samples by a 100× objective lens with an NA of 0.9. The instrumental spectral resolution was 0.5 $cm^{-1}$, and the Si Raman band was used as an internal frequency reference. An integration time of 30 s and spectrometer at 1800 grooves/mm were used during the test.

**Measurements of Pristine and SAM-Modified Few-Layer $MoS_2$ FETs.** Trilayer $MoS_2$ nanoflakes are chosen to be fabricated for FETs because of the relatively larger size. In order to avoid the contamination from photolithography or electron-beam lithography, the traditional shadow mask (Cu grids) was used to fabricate the microelectrodes. Because of the relative lower contact resistance between $MoS_2$ nanoflakes and Al,[14,15] Al electrodes with 200-nm thickness were fabricated by resistance heating evaporation, and the channel length was 6 $\mu$m. Before test, the devices were annealed at 150 °C for 4 h surrounded with Ar gas. Keithley 4200 semiconductor characterization system was used to measure the transfer and output characteristics of the devices on a Lakeshore probe station.

**Surface Potential of $MoS_2$ Nanoflakes.** Surface potential measurement of $MoS_2$ nanoflakes with different layers was conducted by a scanning probe microscope (SPM, Bruker Dimension Icon) with conductive probes (Co/Cr coated tip). The working mechanism of KFM can been seen in previous reference.[43] For the measurement of surface potential, an a.c. amplitude of 900 mV and a liftheight of 60 nm were used. For annealing experiments, pristine $MoS_2$ nanoflakes were annealed at 230 °C for 2 h surrounded with Ar atmosphere, and then the surface potential of annealed $MoS_2$ nanoflakes were measured by KFM.

*Conflict of Interest:* The authors declare no competing financial interest.

*Acknowledgment.* C.Y.X. acknowledges support from the Fundamental Research Funds for the Central Universities (HIT. BRETIII.201203). The authors thank S.Q. Zhang, W. Feng and W.D. Li for Raman spectrum, FET measurements, and language polishing, respectively.

*Supporting Information Available:* Water contact angle and the AFM topography of Si substrate, additional Raman spectra of $MoS_2$ on the pristine and modified substrates, the output and transfer curves of FOTS-modified trilayer $MoS_2$ FETs, the height images of measured $MoS_2$, surface potential maps of $MoS_2$ nanoflakes on the pristine and SAM-modified substrates, the surface potential of $MoS_2$ nanoflakes with different relative humidity and annealing treatment. This material is available free of charge *via* the Internet at http://pubs.acs.org.

## REFERENCES AND NOTES

1. Wilson, J.; Yoffe, A. The Transition Metal Dichalcogenides Discussion and Interpretation of the Observed Optical, Electrical and Structural Properties. *Adv. Phys.* **1969**, *18*, 193–335.
2. Castro Neto, A. Charge Density Wave, Superconductivity, and Anomalous Metallic Behavior in 2D Transition Metal Dichalcogenides. *Phys. Rev. Lett.* **2001**, *86*, 4382–4385.
3. Wang, Q. H.; Kalantar-Zadeh, K.; Kis, A.; Coleman, J. N.; Strano, M. S. Electronics and Optoelectronics of Two-Dimensional Transition Metal Dichalcogenides. *Nat. Nanotechnol.* **2012**, *7*, 699–712.
4. Huang, X.; Zeng, Z.; Zhang, H. Metal Dichalcogenide Nanosheets: Preparation, Properties and Applications. *Chem. Soc. Rev.* **2013**, *42*, 1934–1946.
5. Chhowalla, M.; Shin, H. S.; Eda, G.; Li, L.-J.; Loh, K. P.; Zhang, H. The Chemistry of Two-Dimensional Layered Transition Metal Dichalcogenide Nanosheets. *Nat. Chem.* **2013**, *5*, 263–275.
6. Novoselov, K.; Jiang, D.; Schedin, F.; Booth, T.; Khotkevich, V.; Morozov, S.; Geim, A. Two-Dimensional Atomic Crystals. *Proc. Natl. Acad. Sci. U. S. A.* **2005**, *102*, 10451–10453.
7. Radisavljevic, B.; Radenovic, A.; Brivio, J.; Giacometti, V.; Kis, A. Single-Layer $MoS_2$ Transistors. *Nat. Nanotechnol.* **2011**, *6*, 147–150.
8. Mak, K. F.; Lee, C.; Hone, J.; Shan, J.; Heinz, T. F. Atomically Thin $MoS_2$: A New Direct-Gap Semiconductor. *Phys. Rev. Lett.* **2010**, *105*, 136805.
9. Yin, Z.; Li, H.; Jiang, L.; Shi, Y.; Sun, Y.; Lu, G.; Zhang, Q.; Chen, X.; Zhang, H. Single-Layer $MoS_2$ Phototransistors. *ACS Nano* **2012**, *6*, 74–80.
10. Li, H.; Yin, Z.; He, Q.; Huang, X.; Lu, G.; Fam, D. W. H.; Tok, A. I. Y.; Zhang, Q.; Zhang, H. Fabrication of Single- and Multilayer $MoS_2$ Film-Based Field-Effect Transistors for Sensing NO at Room Temperature. *Small* **2012**, *8*, 63–67.
11. Lee, H. S.; Min, S. W.; Chang, Y. G.; Park, M. K.; Nam, T.; Kim, H.; Kim, J. H.; Ryu, S.; Im, S. $MoS_2$ Nanosheet Phototransistors with Thickness-Modulated Optical Energy Gap. *Nano Lett.* **2012**, *12*, 3695–3700.
12. Choi, W.; Cho, M. Y.; Konar, A.; Lee, J. H.; Cha, G. B.; Hong, S. C.; Kim, S.; Kim, J.; Jena, D.; Joo, J. Phototransistors: High-Detectivity Multilayer $MoS_2$ Phototransistors with Spectral

Response from Ultraviolet to Infrared. *Adv. Mater.* **2012**, *24*, 5902–5902.
13. Léonard, F.; Talin, A. A. Electrical Contacts to One- and Two-Dimensional Nanomaterials. *Nat. Nanotechnol.* **2011**, *6*, 773–783.
14. Popov, I.; Seifert, G.; Tománek, D. Designing Electrical Contacts to $MoS_2$ Monolayers: A Computational Study. *Phys. Rev. Lett.* **2012**, *108*, 156802.
15. Das, S.; Chen, H.-Y.; Penumatcha, A. V.; Appenzeller, J. High Performance Multi-Layer $MoS_2$ Transistors with Scandium Contacts. *Nano Lett.* **2013**, *13*, 100–105.
16. Liu, H.; Neal, A. T.; Ye, P. D. Channel Length Scaling of $MoS_2$ MOSFETs. *ACS Nano* **2012**, *6*, 8563–8569.
17. Fontana, M.; Deppe, T.; Boyd, A. K.; Rinzan, M.; Liu, A. Y.; Paranjape, M.; Barbara, P. Electron-Hole Transport and Photovoltaic Effect in Gated $MoS_2$ Schottky Junctions. *Sci. Rep.* **2013**, *3*, 1634.
18. Qiu, H.; Pan, L.; Yao, Z.; Li, J.; Shi, Y.; Wang, X. Electrical Characterization of Back-Gated Bi-Layer $MoS_2$ Field-Effect Transistors and the Effect of Ambient on Their Performances. *Appl. Phys. Lett.* **2012**, *100*, 123104.
19. Castellanos-Gomez, A.; Cappelluti, E.; Roldán, R.; Agraït, N.; Guinea, F.; Rubio-Bollinger, G. Electric-Field Screening in Atomically Thin Layers of $MoS_2$: The Role of Interlayer Coupling. *Adv. Mater.* **2013**, *25*, 899–903.
20. Li, Y.; Xu, C.-Y.; Zhen, L. Surface Potential and Interlayer Screening Effect of Few-Layer $MoS_2$ Nanoflakes. *Appl. Phys. Lett.* **2013**, *102*, 143110.
21. Ulman, A. Formation and Structure of Self-Assembled Monolayers. *Chem. Rev.* **1996**, *96*, 1533–1554.
22. Schwartz, D. K Mechanisms and Kinetics of Self-Assembled Monolayer Formation. *Annu. Rev. Phys. Chem.* **2001**, *52*, 107–137.
23. DiBenedetto, S. A.; Facchetti, A.; Ratner, M. A.; Marks, T. J. Molecular Self-Assembled Monolayers and Multilayers for Organic and Unconventional Inorganic Thin-Film Transistor Applications. *Adv. Mater.* **2009**, *21*, 1407–1433.
24. Chen, W.; Gao, X. Y.; Qi, D. C.; Chen, S.; Chen, Z. K.; Wee, A. T. S. Surface-Transfer Doping of Organic Semiconductors Using Functionalized Self-Assembled Monolayers. *Adv. Funct. Mater.* **2007**, *17*, 1339–1344.
25. de Boer, B.; Hadipour, A.; Mandoc, M. M.; van Woudenbergh, T.; Blom, P. W. Tuning of Metal Work Functions with Self-Assembled Monolayers. *Adv. Mater.* **2005**, *17*, 621–625.
26. Campbell, I.; Rubin, S.; Zawodzinski, T.; Kress, J.; Martin, R.; Smith, D.; Barashkov, N.; Ferraris, J. Controlling Schottky Energy Barriers in Organic Electronic Devices Using Self-Assembled Monolayers. *Phys. Rev. B* **1996**, *54*, 14321–14324.
27. Park, J.; Lee, W. H.; Huh, S.; Sim, S. H.; Kim, S. B.; Cho, K.; Hong, B. H.; Kim, K. S. Work-Function Engineering of Graphene Electrodes by Self-Assembled Monolayers for High-Performance Organic Field Effect Transistors. *J. Phys. Chem. Lett.* **2011**, *2*, 841–845.
28. Wang, R.; Wang, S.; Zhang, D.; Li, Z.; Fang, Y.; Qiu, X. Control of Carrier Type and Density in Exfoliated Graphene by Interface Engineering. *ACS Nano* **2010**, *5*, 408–412.
29. Shi, Y.; Kim, K. K.; Reina, A.; Hofmann, M.; Li, L. J.; Kong, J. Work Function Engineering of Graphene Electrode *via* Chemical Doping. *ACS Nano* **2010**, *4*, 2689–2694.
30. Yokota, K.; Takai, K.; Enoki, T. Carrier Control of Graphene Driven by the Proximity Effect of Functionalized Self-Assembled Monolayers. *Nano Lett* **2011**, *11*, 3669–3675.
31. Lee, B.; Chen, Y.; Duerr, F.; Mastrogiovanni, D.; Garfunkel, E.; Andrei, E.; Podzorov, V. Modification of Electronic Properties of Graphene with Self-Assembled Monolayers. *Nano Lett.* **2010**, *10*, 2427–2432.
32. Kobayashi, S.; Nishikawa, T.; Takenobu, T.; Mori, S.; Shimoda, T.; Mitani, T.; Shimotani, H.; Yoshimoto, N.; Ogawa, S.; Iwasa, Y. Control of Carrier Density by Self-Assembled Monolayers in Organic Field-Effect Transistors. *Nat. Mater.* **2004**, *3*, 317–322.
33. Hozumi, A.; Ushiyama, K.; Sugimura, H.; Takai, O. Fluoroalkylsilane Monolayers Formed by Chemical Vapor Surface Modification on Hydroxylated Oxide Surfaces. *Langmuir* **1999**, *15*, 7600–7604.
34. Rozlosnik, N.; Gerstenberg, M. C.; Larsen, N. B. Effect of Solvents and Concentration on the Formation of a Self-Assembled Monolayer of Octadecylsiloxane on Silicon (001). *Langmuir* **2003**, *19*, 1182–1188.
35. Wang, Y.; Lieberman, M. Growth of Ultrasmooth Octadecyltrichlorosilane Self-Assembled Monolayers on $SiO_2$. *Langmuir* **2003**, *19*, 1159–1167.
36. Ahn, M. W.; Park, K. S.; Heo, J. H.; Park, J. G.; Kim, D. W.; Choi, K.; Lee, J. H.; Hong, S. H. Gas Sensing Properties of Defect-Controlled ZnO-Nanowire Gas Sensor. *Appl. Phys. Lett.* **2008**, *93*, 263103.
37. Gong, Y.; Wang, M. C.; Zhang, X.; Ng, H. W.; Gates, B. D. Optimizing the Quality of Monoreactive Perfluoroalkylsilane-Based Self-Assembled Monolayers. *Langmuir* **2012**, *28*, 11790–11801.
38. Stenger, D. A.; Georger, J. H.; Dulcey, C. S.; Hickman, J. J.; Rudolph, A. S.; Nielsen, T. B.; McCort, S. M.; Calvert, J. M. Coplanar Molecular Assemblies of Amino- and Perfluorinated Alkylsilanes: Characterization and Geometric Definition of Mammalian Cell Adhesion and Growth. *J. Am. Chem. Soc.* **1992**, *114*, 8435–8442.
39. Lee, C.; Yan, H.; Brus, L. E.; Heinz, T. F.; Hone, J.; Ryu, S. Anomalous Lattice Vibrations of Single- and Few-Layer $MoS_2$. *ACS Nano* **2010**, *4*, 2695–2700.
40. Rice, C.; Young, R.; Zan, R.; Bangert, U.; Wolverson, D.; Georgiou, T.; Jalil, R.; Novoselov, K. Raman-Scattering Measurements and First-Principles Calculations of Strain-Induced Phonon Shifts in Monolayer $MoS_2$. *Phys. Rev. B* **2013**, *87*, 081307.
41. Conley, H. J.; Wang, B.; Ziegler, J. I.; Haglund, R. F., Jr.; Pantelides, S. T.; Bolotin, K. I. Bandgap Engineering of Strained Monolayer and Bilayer $MoS_2$. *Nano Lett.* **2013**, *13*, 3626–3630.
42. Chakraborty, B.; Bera, A.; Muthu, D.; Bhowmick, S.; Waghmare, U.; Sood, A. Symmetry-Dependent Phonon Renormalization in Monolayer $MoS_2$ Transistor. *Phys. Rev. B* **2012**, *85*, 161403.
43. Mao, N.; Chen, Y.; Liu, D.; Zhang, J.; Xie, L. Solvatochromic Effect on the Photoluminescence of $MoS_2$ Monolayers. *Small* **2013**, *9*, 1312–1315.
44. Wang, X.; Xu, J. B.; Wang, C.; Du, J.; Xie, W. High-Performance Graphene Devices on $SiO_2$/Si Substrate Modified by Highly Ordered Self-Assembled Monolayers. *Adv. Mater.* **2011**, *23*, 2464–2468.
45. Lee, W. H.; Park, J.; Kim, Y.; Kim, K. S.; Hong, B. H.; Cho, K. Control of Graphene Field-Effect Transistors by Interfacial Hydrophobic Self-Assembled Monolayers. *Adv. Mater.* **2011**, *23*, 3460–3464.
46. Wang, X.; Xu, J.-B.; Xie, W.; Du, J. Quantitative Analysis of Graphene Doping by Organic Molecular Charge Transfer. *J. Phys. Chem. C* **2011**, *115*, 7596–7602.
47. Palermo, V.; Palma, M.; Samorì, P. Electronic Characterization of Organic Thin Films by Kelvin Probe Force Microscopy. *Adv. Mater.* **2006**, *18*, 145–164.
48. Hayashi, K.; Saito, N.; Sugimura, H.; Takai, O.; Nakagiri, N. Regulation of the Surface Potential of Silicon Substrates in Micrometer Scale with Organosilane Self-Assembled Monolayers. *Langmuir* **2002**, *18*, 7469–7472.
49. Saito, N.; Hayashi, K.; Sugimura, H.; Takai, O.; Nakagiri, N. Surface Potential Images of Self-Assembled Monolayers Patterned by Organosilanes: *ab initio* Molecular Orbital Calculations. *Surf. Interface Anal.* **2002**, *34*, 601–605.
50. Datta, S. S.; Strachan, D. R.; Mele, E.; Johnson, A. C. Surface Potentials and Layer Charge Distributions in Few-Layer Graphene Films. *Nano Lett.* **2008**, *9*, 7–11.
51. Late, D. J.; Liu, B.; Matte, H. R.; Dravid, V. P.; Rao, C. Hysteresis in Single-Layer $MoS_2$ Field Effect Transistors. *ACS Nano* **2012**, *6*, 5635–5641.
52. Schumacher, A.; Kruse, N.; Prins, R.; Meyer, E.; Luthi, R.; Howald, L.; Guntherodt, H. J.; Scandella, L. Influence of Humidity on Friction Measurements of Supported $MoS_2$ Single Layers. *J. Vac. Sci. Technol., B: Microelectron. Nanometer Struct.* **1996**, *14*, 1264–1267.

53. Ziegler, D.; Gava, P.; Güttinger, J.; Molitor, F.; Wirtz, L.; Lazzeri, M.; Saitta, A.; Stemmer, A.; Mauri, F.; Stampfer, C. Variations in the Work Function of Doped Single- and Few-Layer Graphene Assessed by Kelvin Probe Force Microscopy and Density Functional Theory. *Phys. Rev. B* **2011**, *83*, 235434.
54. Oliveira, C.; Matos, M.; Chacham, H.; Neves, B. Anomalous Response of Supported Few-Layer Hexagonal Boron Nitride to DC Electric Fields: A Confined Water Effect? *Nanotechnology* **2012**, *23*, 175703.